

Article

SnO₂-Based Porous Nanomaterials: Sol-Gel Formation and Gas-Sensing Application

Irina Kononova ¹, Vyacheslav Moshnikov ¹  and Pavel Kononov ^{2,*} 

¹ Department of Micro- and Nanoelectronics, Faculty of Electronics, Saint-Petersburg Electrotechnical University “LETI”, 5, pr. Popova, 197022 Saint-Petersburg, Russia

² Department of Descriptive Geometry and Graphics, Faculty of Basic and Human Sciences, Saint-Petersburg Mining University, 2, 21st Line, 199106 Saint-Petersburg, Russia

* Correspondence: kononov_pv@pers.spmi.ru; Tel.: +7-981-201-5259

Abstract: Porous nanocomposites using two (tin dioxide–silica dioxide) and three (tin dioxide–indium oxide–silica dioxide)-component systems for gas sensors were created with the sol–gel method. To understand some of the physical–chemical processes that occurred during the adsorption of gas molecules on the surface of the produced nanostructures, two models—the Langmuir model and the Brunauer–Emmett–Teller theory—were used to carry out calculations. The results of the phase analysis concerning the interaction between the components during the formation of the nanostructures were obtained through the use of X-ray diffraction, thermogravimetric analysis, the Brunauer–Emmett–Teller technique (to determine the surface areas), the method of partial pressure diagrams in a wide range of temperatures and pressures and the results of the measurement of the nanocomposites’ sensitivity. The analysis allowed us to find the optimal temperature for annealing nanocomposites. The introduction of a semiconductor additive into a two-component system based on tin and silica dioxides significantly increased the sensitivity of the nanostructured layers to reductional reagent gases.

Keywords: sol–gel process; porous nanocomposites; tin dioxide; indium oxide; gas sensitivity



Citation: Kononova, I.; Moshnikov, V.; Kononov, P. SnO₂-Based Porous Nanomaterials: Sol-Gel Formation and Gas-Sensing Application. *Gels* **2023**, *9*, 283. <https://doi.org/10.3390/gels9040283>

Academic Editors: Andrei Jitianu, Robert Edward Przekop, Bogna Sztorch and Eliza Romanczuk-Ruszuk

Received: 10 February 2023

Revised: 13 March 2023

Accepted: 24 March 2023

Published: 31 March 2023



Copyright: © 2023 by the authors. Licensee MDPI, Basel, Switzerland. This article is an open access article distributed under the terms and conditions of the Creative Commons Attribution (CC BY) license (<https://creativecommons.org/licenses/by/4.0/>).

1. Introduction

The introduction of nanotechnologies has allowed us to design completely new composite, constructive and functional nanomaterials [1–4] with considerably improved physical and chemical properties [5–17]. One of the fastest-growing directions in nanotechnologies concerns the development of functional porous materials based on metal oxide [18].

Functional, porous materials based on metal oxide can be obtained through the use of the sol–gel method [19,20], which deals with substances in their liquid state at the synthesis stage and homogenizes the initial components at the molecular level. Sol–gel technology [21] refers to economical and environmentally friendly technologies. Sol–gel thermodynamically nonequilibrium processes are widely used in the field of nanotechnologies [22–25]. At all stages of the sol–gel processes, diverse reactions that influence the composition and structure of the xerogel take place. It has been shown that the basis of sol–gel methods is the production of a homogeneous sol from the precursors and its conversion into a gel. The solvent in the gel is then removed from the gel structure and the remaining gel is dried. The properties of the dried gel significantly depend on the drying method. In other words, the “removing solvent method” is selected according to the application for which the gel is to be used [26–28].

As a rule in microelectronics, sol–gel technologies produce layers that have to meet smoothness and homogeneity requirements. When it comes to using gas-sensitive sensors, obtaining nanocomposite layers with controlled and replicable pore sizes is of high interest. In this case, nanocomposite materials have to contain an adhesion-improving phase and one or more phases of semiconductor n-type (conductivity) metal oxides to ensure gas

sensitivity [29–31]. Metal oxide semiconductor compounds of n-type electrical conductivity, such as SnO₂, ZnO, TiO₂, WO₃, Fe₂O₃, NiO and In₂O₃, are used as primary sensing elements in sensor devices. Of the listed materials, SnO₂ is the most promising material for creating semiconductor gas sensors.

Tin oxide [32–34] as a semiconductor metal oxide has revealed great potential in the field of gas sensing due to its porous structure and reduced size. Especially for tin oxide and its composites, their inherent properties, such as high surface areas and unique semiconducting properties with tunable band gaps, make them compelling for sensing applications [35–40]. The electrical conductivity of tin dioxide is very sensitive to the state of surfaces in the region of elevated temperatures, at which redox reactions occur on the surface of the oxides. It is important to note that the high adsorption capacity, which is due to the presence of free electrons in the conduction band of the semiconductor, surface and oxygen vacancies, plays a significant role in chemisorption centres for atmospheric oxygen.

Film structures based on tin dioxide have high mechanical strength and chemical resistance. The destruction of films occurs only when they are exposed to HF or during prolonged processing in alkali.

Resistive gas sensors are considered promising candidates for gas detection, benefiting from their small size, ease of fabrication and operation convenience [41–43]. The way semiconductor gas sensors built onto percolating structures of metal oxide layers work is based on changes in the electrophysical properties during the adsorption of charged forms of oxygen, and the desorption of products of reactions between these layers and molecules of reductional gases [44–46].

The sol–gel method allows us to create porous materials with a large surface area, which can be used for gas sensors. Gas-sensitive porous nanomaterials can contain several types of pores simultaneously (macro–meso–microporous systems). It should be noted that, according to the IUPAC recommendation, three main types of pores are generally distinguished, i.e., micropores of sizes below 2 nm, mesopores in sizes ranging from 2 to 50 nm and macropores of sizes over 50 nm. This classification is based on differences in the basic mechanisms of sorption processes that take place in pores of different sizes.

In refs. [47,48], it is shown that the analytical capabilities of atomic force microscopy do not allow for the diagnosis of elements with sizes smaller than the locality of the method; therefore, the micropore system (less than 2 nm in size) cannot be detected. At the same time, the contribution of such pores to the total surface area can be determined by using the BET technique. To determine the surface area of the scanned areas using AFM, a technique based on the triangulation method was developed. The essence of the technique consists of the sequential approximation of the surface of the investigated area by a set of triangles, and then measuring their area. The area of the scanned area was calculated as the sum of the areas of 130,050 triangles with vertex coordinates corresponding to the coordinates of the vertices of 65,025 squares into which the AFM image was divided. It was found that the surface area of the porous nanocomposites calculated by processing atomic force images differed by 2–3 orders of magnitude from the surface area calculated according to the BET data. This indicated the existence of a micropore system of less than 10 nm, which was not diagnosed using AFM [47,48].

The purpose of this work was to create two types of sol–gel porous xerogels (two-component porous nanocomposites, SiO₂–SnO₂, and three-component porous nanocomposites, SiO₂–SnO₂–In₂O₃) to study the obtained samples with the use of different methods, to select the optimal annealing temperatures of three-component sol–gel systems (SiO₂–SnO₂–In₂O₃), to propose two sensor layer models with pores of different sizes and to create highly sensitive sensor layers.

2. Results and Discussion

The thermal treatment of nanocomposites in a SiO₂–SnO₂–In₂O₃ system can trigger some undesirable (in terms of the formation of nanostructured layers) chemical processes. That is why during the work, a phase analysis of the component interaction processes using

the X-ray phase and thermogravimetric analysis (TGA) methods was conducted, as well as an analysis based on building a partial pressure diagram for a wide range of temperatures and pressures (since an X-ray phase analysis does not yield information about the X-ray amorphous phase of silica dioxide).

2.1. Thermodynamic Analysis of Phase Equilibriums in $\text{SiO}_2\text{-SnO}_2\text{-In}_2\text{O}_3$ System through the Construction of Partial Pressure Diagram

The construction of a partial pressure diagram (PPD) was based on an analysis of the conditions of an equilibrium in a heterogeneous chemical reaction in the presence of gas-like substances. The PPD showed areas of resistance or a condensed phase depending on the composition of the gas phase, as well as the isothermal cross-sections of the PPD of three-component systems, including a gas phase consisting of two gases. As a result of the X-ray phase analysis, the condensed phases of such a system were either in a solid or liquid state and did not form solid solutions. Phase equilibriums in a Sn–Si–In–O system can be represented in a geometrical way using an N-dimension space, with N being greater than three, but in order to simplify the calculations and provide it in a more graphic way, the system was divided into three subsystems. It is known [49] that the vapour pressure of Si, SiO and SiO_2 above the solid phase of SiO_2 is considerably lower than the pressure of SnO vapours above solid SnO_2 . This way, in the gas phase, except for oxygen, gaseous SnO was prevalent over composite materials consisting of SnO_2 and SiO_2 , that is why the PPD for the Sn–Si–O subsystem was built within the $\lg P_{\text{O}_2}\text{-lg} P_{\text{SnO}}$ coordinates (the half-logarithmic temperature dependence of SnO ($\lg P_{\text{SnO}} = f(T)$) vapour pressures is shown in Table 1). Since all the processes took place in air (at atmospheric pressure), it was assumed that $P_{\text{O}_2} = 0.21$ atm. The reagents were chosen and the chemical interaction equation system was built in such a way that at least one gaseous component was part of the equilibrium (Table 2). It was known [49] that the pressure of InO and In_2O vapours above the solid phase of In_2O_3 and Si, SiO and SiO_2 above the solid phase of SiO_2 was significantly lower than the pressure of In vapours above solid In_2O_3 . This way, in the gas phase, gaseous In was prevalent over composite materials consisting of In_2O_3 and SiO_2 , which is why the PPD for the In–Si–O subsystem was built within the $\lg P_{\text{O}_2}\text{-lg} P_{\text{In}}$ coordinates (the half-logarithmic temperature dependence $\lg P_{\text{In}} = f(T)$ is shown in Table 3). The choice of reagents and the composition of the equation system of their interactions in the In–Si–O subsystem are shown in Table 4. The PPD for the In–Sn–O was built within the $\lg P_{\text{O}_2}\text{-lg} P_{\text{In}}$ and $\lg P_{\text{O}_2}\text{-lg} P_{\text{SnO}}$ coordinates. The choice of reagents and the construction of the equation system of their interactions in the In–Sn–O are shown in Table 5. The calculations of the reaction constants were performed using the standard thermodynamic procedure with the following ratios:

$$\Delta G_T^0 = \Delta H_{298}^0 + \int_{298}^T \Delta C_p^0 dT - T \left(\Delta S_{298}^0 + \int_{298}^T \frac{\Delta C_p^0}{T} dT \right) \quad (1)$$

$$\Delta G_T^0 = -RT \ln K_p,$$

where ΔH_{298}^0 is the change in the standard reaction enthalpy, ΔS_{298}^0 is the change in the standard reaction entropy, ΔC_p^0 in the change in the heat capacity (the thermodynamic characteristics in the Sn–Si–In–O system are shown in Table 6), ΔG_T^0 is the change in free Gibbs energy, K_p is the equilibrium constant and T is the temperature. The value of ΔC_p^0 for the monovariant equilibriums was small, which is why the calculations were conducted using the Ulich approximation: $\Delta C_p^0 = \Delta C_p^0_{298}$. The results of the calculations of the equilibrium constants of the chemical interactions are shown in Table 6 and in Figures 1–8.

Table 1. Temperature dependency $\lg P_{\text{SnO}} = f(T)$.

T, K	400	505	1000	1250
$-\lg P_{\text{SnO}}$	42.165	31.345	11.153	7.284

Table 2. Phase equilibriums in Sn–Si–O system.

Coexisting Phases	Reactions
Si, SiO ₂	Si _(s) + O _{2(g)} = SiO _{2(s)}
SiO ₂ , SnSiO ₃	SiO _{2(s)} + SnO _(g) = SnSiO _{3(s)}
Si, SnSiO ₃	Si _(s) + O _{2(g)} + SnO _(g) = SnSiO _{3(s)}

Table 3. Temperature dependency $\lg P_{\text{In}} = f(T)$.

T, K	373	573	1000	1500
$-\lg P_{\text{In}}$	47.58	28.58	13.073	6.466

Table 4. Phase equilibriums in In–Si–O system.

Coexisting Phases	Reactions
Si, SiO ₂	Si _(s) + O _{2(g)} = SiO _{2(s)}
Si, In ₂ (SiO ₃) ₃	3Si _(s) + 2In _(g) + 9/2O _{2(g)} = In ₂ (SiO ₃) _{3(s)}
SiO ₂ , In ₂ (SiO ₃) ₃	3SiO _{2(s)} + 2In _(g) + 3/2O _{2(g)} = In ₂ (SiO ₃) _{3(s)}

Table 5. Phase equilibriums in In–Sn–O system.

Coexisting Phases	Reactions
Sn, SnO ₂	Sn _(s) + O _{2(g)} = SnO _{2(s)}
In, In ₂ O ₃	2In _(s) + 3/2O _{2(g)} = In ₂ O _{3(s)}

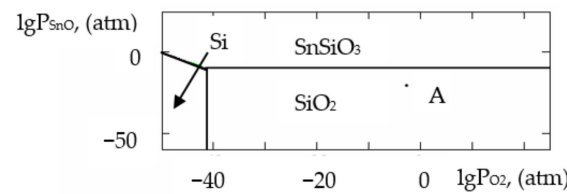


Figure 1. PPD in Sn–Si–O system at temperature T = 873 K within $\lg P_{\text{O}_2}$ – $\lg P_{\text{SnO}}$ coordinates.

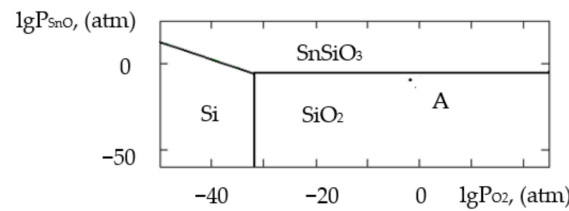


Figure 2. PPD in Sn–Si–O system at temperature T = 1073 K within $\lg P_{\text{O}_2}$ – $\lg P_{\text{SnO}}$ coordinates.

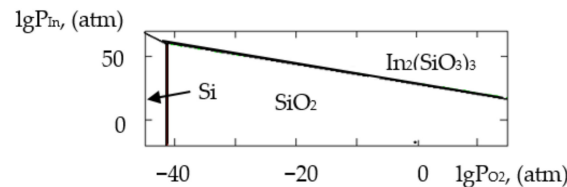


Figure 3. PPD in In–Si–O system at temperature T = 873 K within $\lg P_{\text{O}_2}$ – $\lg P_{\text{In}}$ coordinates.

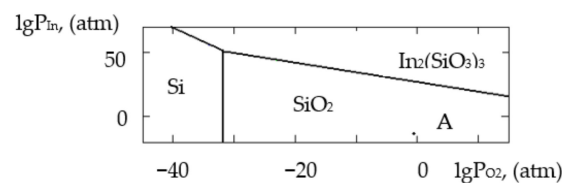


Figure 4. PPD in In–Si–O system at temperature T = 1073 K within $\lg P_{\text{O}_2}$ – $\lg P_{\text{In}}$ coordinates.

Table 6. Results of calculations of equilibrium reaction constants.

Subsystem, Reaction and Equilibrium Equation Line	T, K	lgK _p
Sn-Si-O: Si _(s) + O _{2(g)} = SiO _{2(s)} lgP _{O₂} = -lgK _p	873 1073	41.365 31.872
SiO _{2(s)} + SnO _(g) = SnSiO _{3(s)} lgP _{SnO} = -lgK _p	873 1073	9.385 5.503
Si _(s) + O _{2(g)} + SnO _(g) = SnSiO _{3(s)} lgP _{SnO} = -lgP _{O₂} - lgK _p	873 1073	50.738 37.365
In-Si-O: Si _(s) + O _{2(g)} = SiO _{2(s)} lgP _{O₂} = -lgK _p	873 1073	41.365 31.872
3Si _(s) + 2In _(g) + 9/2O _{2(g)} = In ₂ (SiO ₃) _{3(s)} 2lgP _{In} = -9/2 lgP _{O₂} - lgK _p	873 1073	66.497 41.549
3SiO _{2(s)} + 2In _(g) + 3/2O _{2(g)} = In ₂ (SiO ₃) _{3(s)} 2lgP _{In} = -3/2 lgP _{O₂} - lgK _p	873 1073	-57.603 -54.103
In-Sn-O: Sn _(s) + O _{2(g)} = SnO _{2(s)} lgP _{O₂} = -lgK _p	873 1073	24.025 17.526
2In _(s) + 3/2O _{2(g)} = In ₂ O _{3(s)} lgP _{O₂} = -2/3 lgK _p	873 1073	38.791 28.434
Calculations of pressures of saturated vapours		
Sn-Si-O, In-Sn-O: SnO _(s) = SnO _(g) LgP _{SnO} = lgK _p	873 1073	-8.254 -4.503
In-Si-O, In-Sn-O: In _(s) = In _(g) LgP _{In} = lgK _p	873 1073	-8.637 -5.965

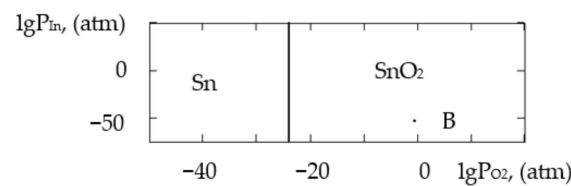


Figure 5. PPD in In-Sn-O system at temperature T = 873 K within lgP_{O₂}-lgP_{In}.

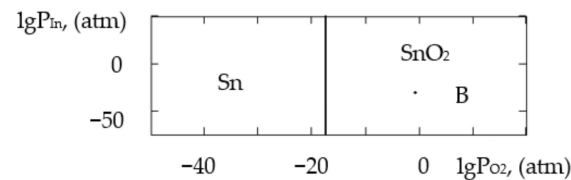


Figure 6. PPD in In-Sn-O system at temperature T = 1073 K within lgP_{O₂}-lgP_{In}.

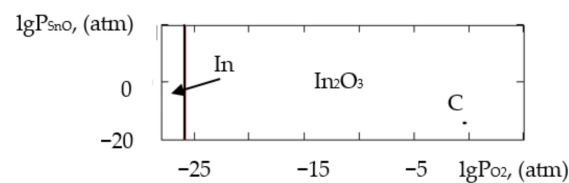


Figure 7. PPD in In-Sn-O system at temperature T = 873 K within lgP_{O₂}-lgP_{SnO}.

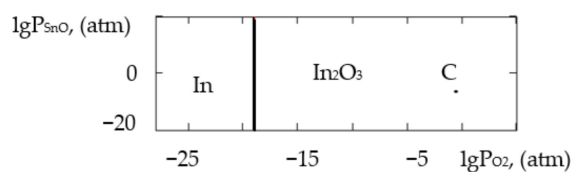


Figure 8. PPD in In–Sn–O system at temperature $T = 1073$ K within $\lg P_{O_2}$ – $\lg P_{SnO}$.

The calculations of the pressures of the saturated SnO and In vapours are shown in Table 6. The vapours of SnO and In in the Sn–Si–O, In–Si–O and In–Sn–O systems were only present in the gas phase at partial pressures lower than those in Table 6; if those pressures were reached, the gaseous components would condense. From the PPD in the Sn–Si–In–O system, it followed that under the conditions of the experiment (at the atmospheric pressure and studied temperature), the next were stable:

- The phase of amorphous SiO_2 (point A, Figures 1–4);
- The phase of crystalline SnO_2 (point B, Figures 5 and 6);
- The phase of crystalline In_2O_3 (point C, Figures 7 and 8).

2.2. Studying the Xerogel Powder Samples Using XRD, TGA and BET

The features of nanocomposites were studied using gel powders produced from the initial gel. The results of the study conducted using the X-ray phase analysis method in SiO_2 , SnO_2 and In_2O_3 systems are shown in Figures 9 and 10.

An analysis of the X-ray phase analysis data for the nanocomposite powders ($10SiO_2$ – $85SnO_2$ – $5In_2O_3$, $10SiO_2$ – $80SnO_2$ – $10In_2O_3$ and $10SiO_2$ – $80SnO_2$ – $10In_2O_3$ (mas. %)) showed that after a thermal treatment at 300 °C (Figure 9), the peaks of the $SnCl_2$ and $InCl_3$ phases occurred, as well as peaks reflecting the initial crystallization of the SnO_2 and In_2O_3 phases. As the concentration of indium salts in the sample grew, the general appearance of the diffractograms stayed the same, but a widening of peaks in the $InCl_3$ phase alongside a decrease in their intensity was noticed, as well as a more pronounced crystallization of the SnO_2 phase. It may be assumed that chloride anions were captured by positively charged ions of indium. During this, the released tin ions actively interacted with oxygen atoms, as a result of which SnO_2 crystallites were formed. After a treatment at 600 °C, the $SnCl_2$ phase peaks disappeared completely, but the $InCl_3$ phase peaks remained, and well-formed SnO_2 phase peaks appeared (SnO_2 (110), SnO_2 (101), SnO_2 (200), SnO_2 (211) and SnO_2 (002)), while the intensity of the In_2O_3 phase reflexes decreased (In_2O_3 (411), In_2O_3 (440) and In_2O_3 (600)). At the same time, as the concentration of indium salts grew, the general appearance of the diffractograms remained the same, but the SnO_2 phase peaks widened, even in the small angle section, which indicated that the size of the SnO_2 crystallites decreased. After a treatment at 700 °C, only the SnO_2 and In_2O_3 phase peaks remained (Figure 11). The size of the crystallites was estimated with the Scherrer equation, and was equal to 17–37 nm.

According to the results of the TGA, at 100 °C (Figure 12a), endothermic effects occurred associated with a mass loss of 79% and the simultaneous crystallization of the material. This was confirmed using the XRD data; already at 300 °C, the crystallization of the SnO_2 phase could be observed. The thermogravigram at 600 °C (Figure 12b) reflected a mass loss of 17% against the background of an exoeffect, indicating the continued crystallization of SnO_2 and In_2O_3 .

The specific surface areas of the nanocomposites were studied. A thermal conductivity sensor was used as a detector of the composition of the gas mixture, the output signal of which was a desorption peak (Figure 13) and the area of which was directly proportional to the volume of the desorbed gas. According to the results of the BET method, it was found that the specific surface area of the two-component system (tin dioxide–silica dioxide) was 80 – 100 m^2/g . The surface area for the three-component system (tin dioxide–indium oxide–silica dioxide) was several times larger than the component in the two-component system.

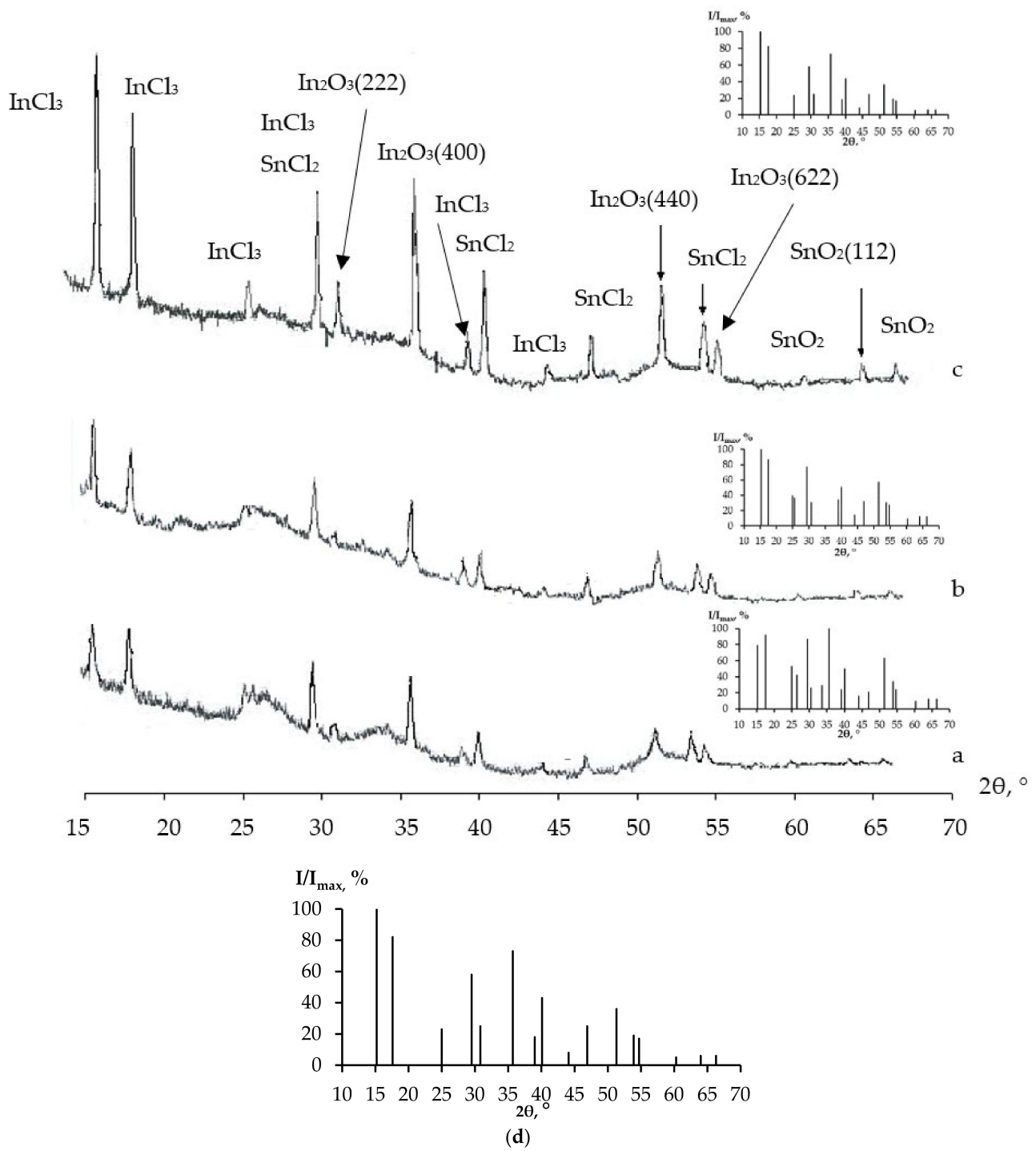


Figure 9. Cont.

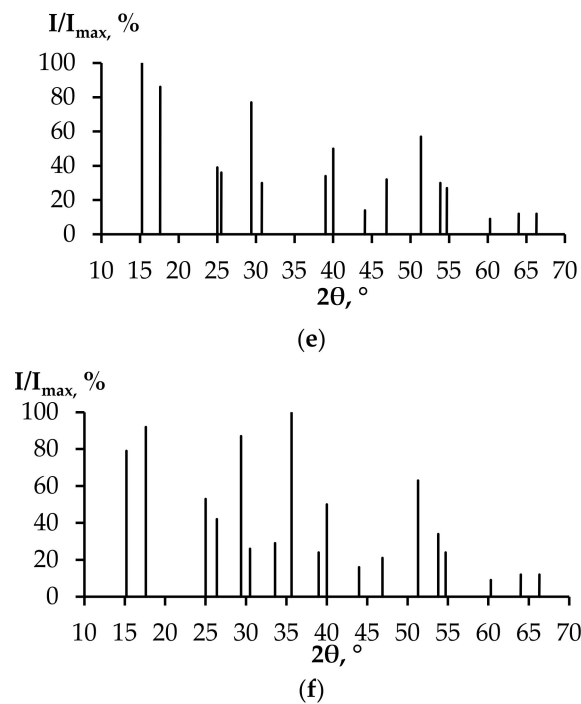


Figure 9. XRD patterns (after thermal treatment at 300 °C) showing the intensity of diffracted X-rays in planes as a function of 2θ for three samples: (a,f) $10\text{SiO}_2\text{-}85\text{SnO}_2\text{-}5\text{In}_2\text{O}_3$; (b,e) $10\text{SiO}_2\text{-}80\text{SnO}_2\text{-}10\text{In}_2\text{O}_3$; (c,d) $10\text{SiO}_2\text{-}75\text{SnO}_2\text{-}15\text{In}_2\text{O}_3$ (the Miller indices (hkl) are also shown beside the peaks).

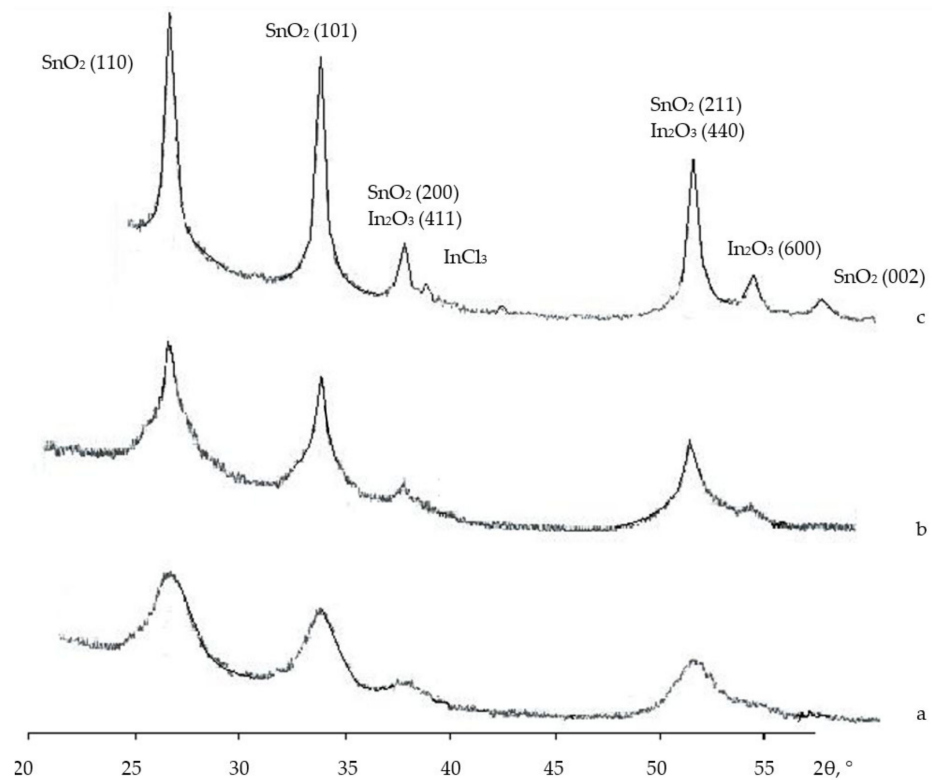


Figure 10. Cont.

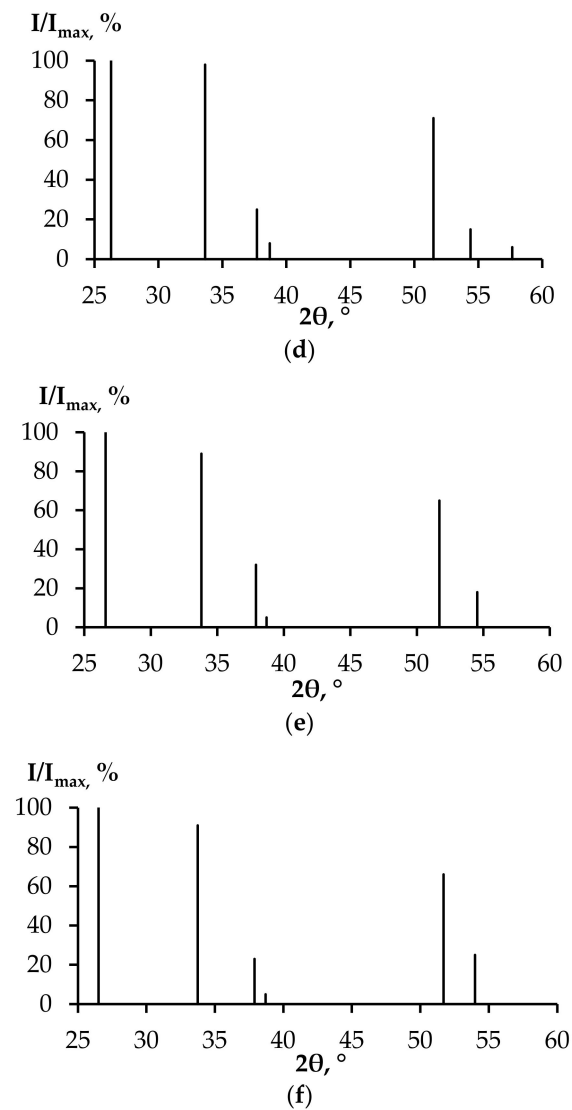


Figure 10. XRD patterns (after thermal treatment at 600 °C) showing the intensity of diffracted X-rays in planes as a function of 2θ for three samples: (a,f) 10SiO₂-85SnO₂-5In₂O₃; (b,e) 10SiO₂-80SnO₂-10In₂O₃; (c,d) 10SiO₂-75SnO₂-15In₂O₃ (the Miller indices (hkl) are also shown beside the peaks).

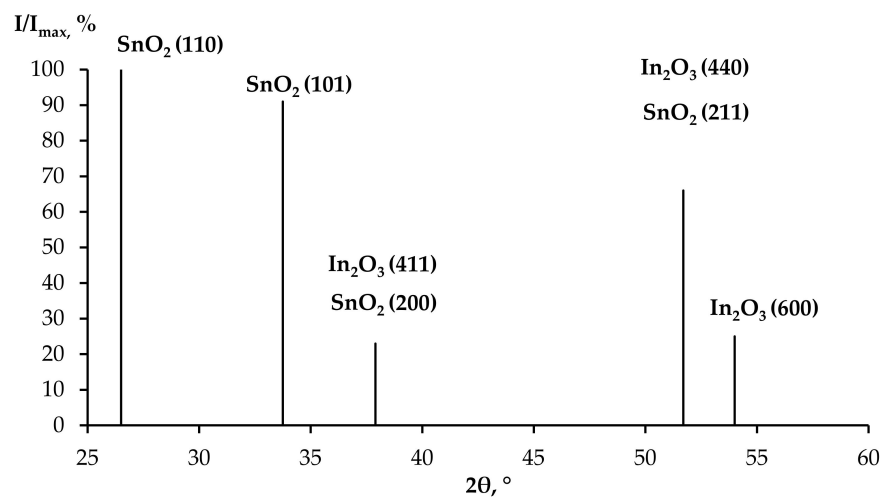


Figure 11. Typical XRD pattern (after thermal treatment at 700 °C).

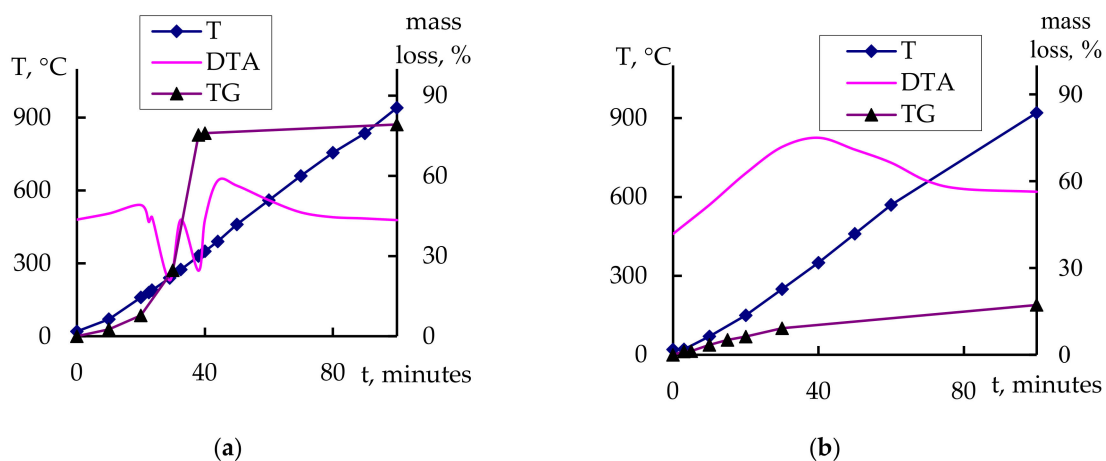


Figure 12. TGA curves: (a) after heat treatment at 100 °C for 50 h; (b) after heat treatment at 100 °C for 50 h and 600 °C for 1 h ($10\text{SiO}_2\text{-}75\text{SnO}_2\text{-}15\text{In}_2\text{O}_3$).

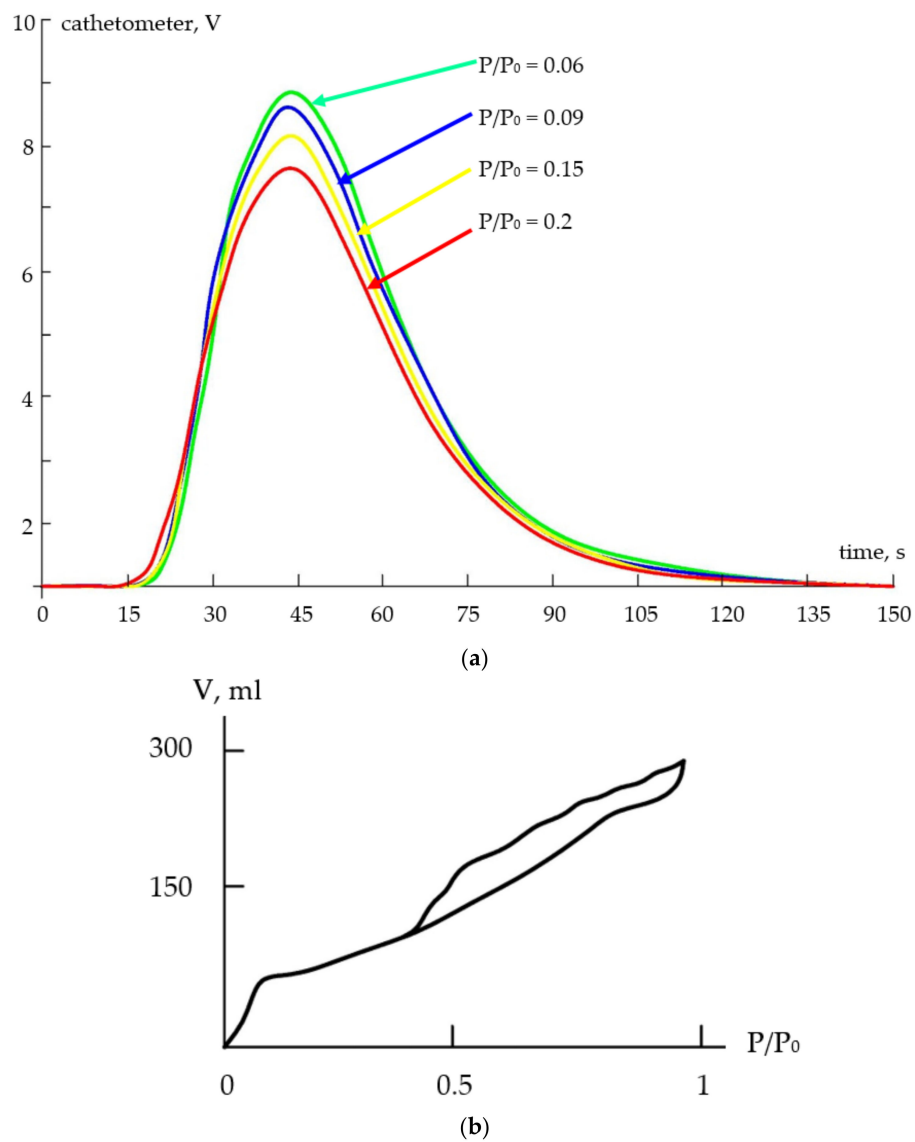


Figure 13. (a) Signals received from thermal conductivity meter formed during adsorption analysis; (b) a typical adsorption isotherm.

2.3. Studying the Morphology of the Xerogel Films

The morphology of the porous nanocomposites of two- and three-component systems (tin dioxide–silica dioxide and tin dioxide–indium oxide–silica dioxide) synthesized from sols were studied with the use of AFM. Typical atomic force microscopy images of porous nanocomposites are shown in Figure 14. It was shown that when indium oxide was introduced into a two-component structure, the pore sizes significantly decreased from 60–170 nm to 10 nm.

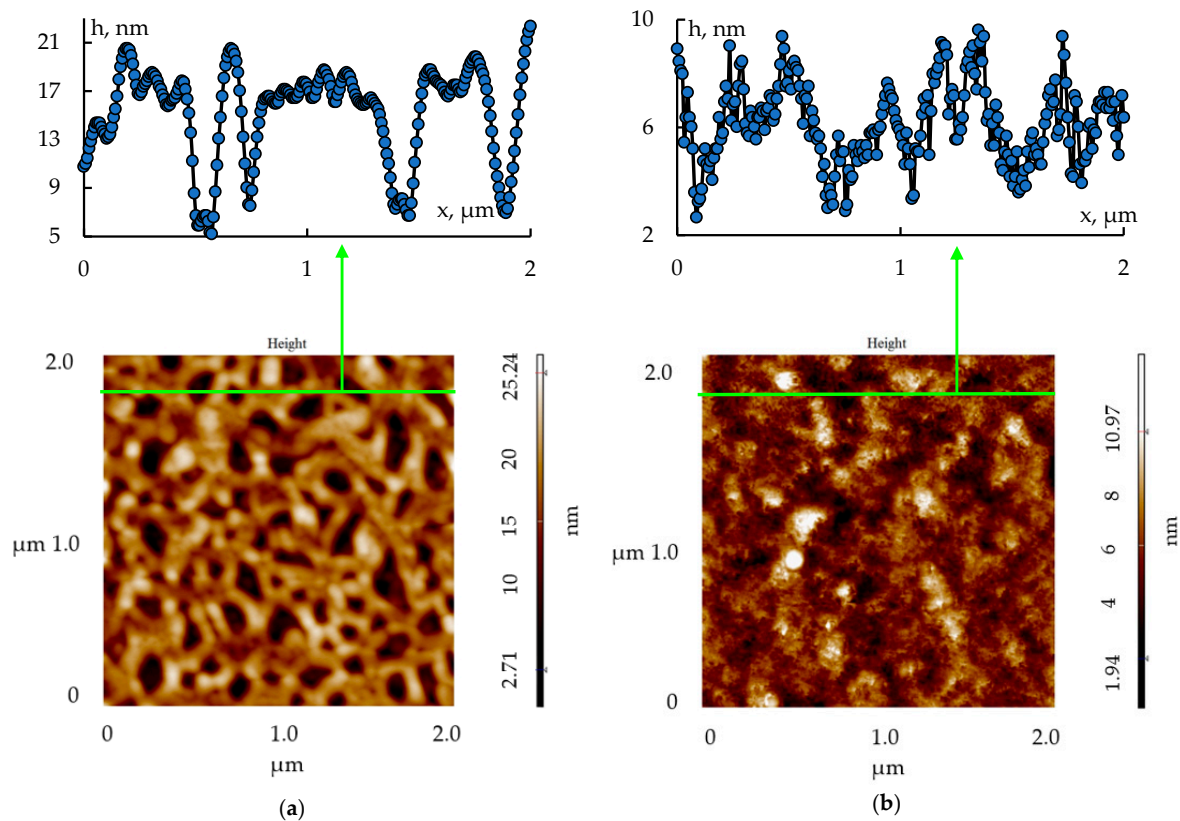


Figure 14. Typical atomic force microscopy images (image size $2\ \mu\text{m} \times 2\ \mu\text{m}$) of porous nanocomposites and their profiles (along the green lines): (a) a two-component system, $\text{SiO}_2\text{-SnO}_2$; (b) a three-component system, $\text{SiO}_2\text{-SnO}_2\text{-In}_2\text{O}_3$.

2.4. Studying the Electrophysical Properties of Film Nanocomposites

When studying the electrophysical properties, it was found that the resistance of structures decreased as the temperature rose, according to the exponential law:

$$R = R_0 \exp\left(\frac{E_A}{kT}\right). \quad (2)$$

where R is the resistance of the sample, R_0 is the typical value for this sample, $k = 8.615 \cdot 10^{-5}$ eV/K is the Boltzmann constant, T is the temperature and E_A is the activation energy, which confirmed the semiconductor characteristic of the conductivity of the metal oxide structures. Using temperature dependencies (in the range of 300–400 °C, Figure 15), the activation energies of the conductivity of semiconductor nanocomposite materials were calculated (which were found to be 0.24–0.46 eV), as well as the temperature resistance coefficients equal to the relative change of the resistance when the temperature changed by 1 K, and was equal to:

$$\alpha_R = \frac{1}{R} \frac{\partial R}{\partial T} = -(6 \div 11) \cdot 10^{-3} \text{K}^{-1} \quad (3)$$

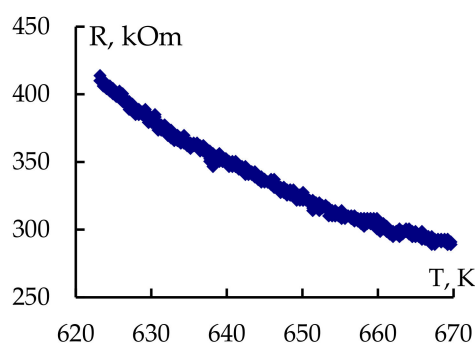


Figure 15. Typical image of temperature dependency of net-like sample produced using sol-gel method.

It must be noted that the experimentally found activation energy could have been the so called 'seeming' activation energy differing from the thermal activation of charge carriers by the value of the thermal effect accompanying the process of oxygen adsorption on the surface of the semiconductor nanocomposites and connected with the existence of a potential barrier to the flow of electricity existing on the grain boundaries.

Figure 16 shows the typical change in the resistance of the sample under the impulse of reagent gas and the further change in the resistance during reduction. The research carried out to determine the sensitivity to acetone and ethanol fumes showed that the reduction time after the impulse was 2–40 min, depending on the detection temperature and sample structure. It was established that a temporary resistance reduction in semiconductor nanocomposites after the impulse of a reagent gas could be performed by sending a thermal (600 °C) impulse for 30 s; in this case, the sensitivity to reagent gases under the same detection conditions could increase 1.5–4 times due to the OH desorption from the surface and higher R_{AIR} .

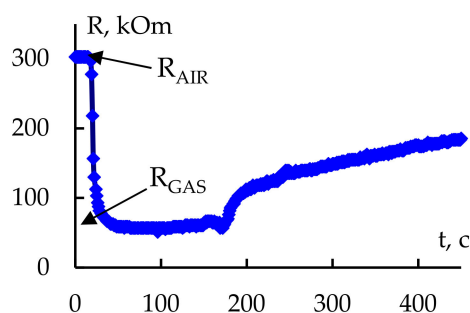


Figure 16. Typical temporal dependency of resistance of net-like nanocomposite during and just after introduction of reagent gas.

2.5. Analysis of Adsorption Processes on Nanocomposite Surfaces

When studying the resistance patterns of nanocomposites based on tin and silica dioxides in a constant electric field in an air environment in the presence of reductional fumes of ethanol and acetone, it was found that as the temperature increased, the reaction time decreased for some samples, while staying the same for others. To interpret the results, software compatible with the LabVIEW environment was developed using simplified traditional models of monomolecular adsorption on a homogeneous surface, which was produced without taking the interaction between adsorbents into consideration (the Langmuir model), as well as those of polymolecular adsorption based on monomolecular adsorption and taking 'vertical' intermolecular adsorbent interactions into account (the BET model).

Within the Langmuir model, the following assumptions were used: adsorption happened in separate adsorption centres, each of which could only retain one molecule of gas; the surface was energy-homogeneous, i.e., it only contained adsorption centres with the

same adsorption heat bond energy between particular molecules of adsorbed gas; adsorbed molecules did not interact, and the strength of the bond between the molecule and the centre did not depend on the filling of adjacent centres; the number of adsorption centres on the surface was constant and did not depend on external conditions; each adsorption centre could only bond to the given molecule in one particular way; the bond energy was constant during the whole life span of the molecule in the adsorption centre.

Within the BET model, it was assumed that each particle of the first monolayer was the adsorption centre for the second layer, etc.; in all layers, except the first, the adsorption heat was equal to the condensation heat; in all layers, except the first, the condensation and evaporation conditions were the same; at a pressure equal to the pressure of the saturated vapours, adsorbed molecules condensed on the surface as a liquid, i.e., the number of layers became infinite.

This way, within the Langmuir model in the LabVIEW environment, the calculations were reduced to analytically solving a first-order linear partial differential equation:

$$\frac{\partial \theta(t)}{\partial t} + (K_{ADS} + K_{DES}) \cdot \theta(t) = K_{ADS} \quad (4)$$

which looked like this:

$$\theta(t) = \exp(-\{K_{ADS} + K_{DES}\} \cdot t) \cdot K_{ADS} \cdot \left[\frac{1}{K_{ADS} + K_{DES}} \cdot \exp(\{K_{ADS} + K_{DES}\} \cdot t) + C \right] \quad (5)$$

where $C = -\frac{1}{K_{ADS} + K_{DES}}$, $K_{ADS} = \frac{p}{N_C \sqrt{2\pi} \cdot M \cdot K_B \cdot T} \cdot \exp\left(-\frac{E_{ADS}}{K_B T}\right)$ is the adsorption coefficient, $K_{DES} = \nu \cdot \exp\left(-\frac{E_{DES}}{K_B T}\right)$ is the desorption coefficient, E_{ADS} and E_{DES} are the adsorption and desorption activation energies, T is the temperature, K_B is the Boltzmann constant, ν is the frequency of attempts to penetrate the desorption barrier, M is the mass of the adsorbed molecule, N_C is the total concentration of occupied and empty spaces (concentration of adsorption centres on the surface), p is the steam pressure, $\theta(t)$ is the degree of the filling of the surface with adsorbed molecules and t is the filling time with adsorbed molecules.

That is why within the BET model in the LabVIEW environment, the calculations were reduced to solving a first-order partial differential equation using the Euler method, in which the right half was a cubic equation related to the degree of the filling of the surface with single complexes at a particular moment of time:

$$\begin{aligned} \frac{\partial \theta^1(t)}{\partial t} = & -K_{ADS} \cdot \left(\frac{p}{p_s}\right)^2 \cdot \{\theta^1(t)\}^3 + \\ & + \left[K_{ADS} \cdot \left(\frac{p}{p_s}\right)^2 - 2 \cdot \left(1 - \frac{p}{p_s}\right) \cdot \frac{p}{p_s} \cdot K_{ADS} - \frac{K_{DES}}{1 - \frac{p}{p_s}} \cdot \frac{p}{p_s} \right] \{\theta^1(t)\}^2 + \\ & + \left[K_{ADS} \cdot 2 \cdot \left(1 - \frac{p}{p_s}\right) \cdot \frac{p}{p_s} - \left(1 - \frac{p}{p_s}\right)^2 \cdot K_{DES} - K_{DES} \right] \cdot \theta^1(t) + \\ & + K_{ADS} \cdot \left(1 - \frac{p}{p_s}\right)^2 \end{aligned} \quad (6)$$

where p_s is the pressure of the saturated gas and $\theta^1(t)$ is the degree of the surface filling with single complexes.

Within the used models, the maximum possible degree of the filling of adsorption centres and the speed of the filling were affected by such parameters as the pressure, temperature, mass of adsorbed molecules and the energies of adsorption and desorption activation (Figure 17).

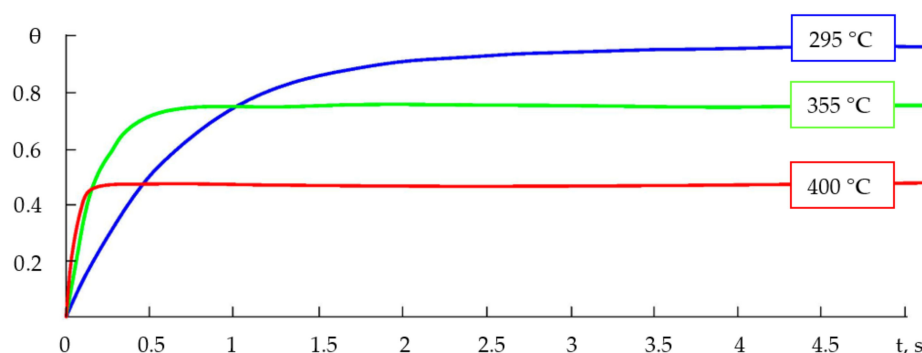


Figure 17. Typical dependencies of degree of filling on time (at different temperatures within Langmuir model).

Based on the results of calculations in the LabVIEW environment, it was found that raising the temperature in one range resulted in a decrease in the amount of time needed to complete the adsorption processes (finding an equilibrium), while, in another temperature range (relatively higher), it led to a decrease in the degree of the filling of the surface with adsorbed particles and the filling time. With the other parameters of the system being equal, both the Langmuir and BET systems (Figures 17 and 18) produced similar correlations between the degree of filling and time, and differed mostly in the filling time; then, since the calculations within the monomolecular model were more trivial, the further analysis of the features of the dependencies of the degree of gas molecule filling was conducted within the Langmuir model.

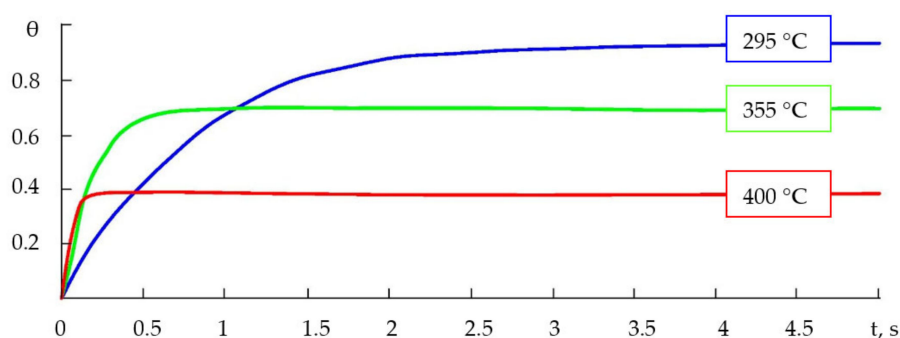


Figure 18. Typical dependencies of degree of filling on time (at different temperatures within BET model).

Comparing the experimental gas sensitivity data to the results of computer modelling showed the existence of an optimal temperature range for the detection process, outside which the degree of the surface filling in a particular adsorber–adsorbent system decreased, and which was found to be between 300 and 400 °C (573–673 K) (Figure 19a). At temperatures close to room temperature, the adsorption process would proceed quite slowly; for example, at room temperature (293 K), the adsorption of ethanol vapours could take up to 3 h, in which case, the filling degree would be $\theta = 0.2$ (within the Langmuir and BET models). It was shown that the filling degree depended on the mass of the molecule—the heavier the molecule, the lower the degree (Figure 19b).

It was also found that for samples characterized by a decrease in sensitivity to reductional gases and reaction time, the typical ratio of ‘effective’ activation temperatures of adsorption and desorption was 2.5 to 1, while for porous nanocomposites characterized by the same sensitivity to reductional gases and an insignificant change in reaction time when the temperature rose, the ratio was more than 3.5 to 1.

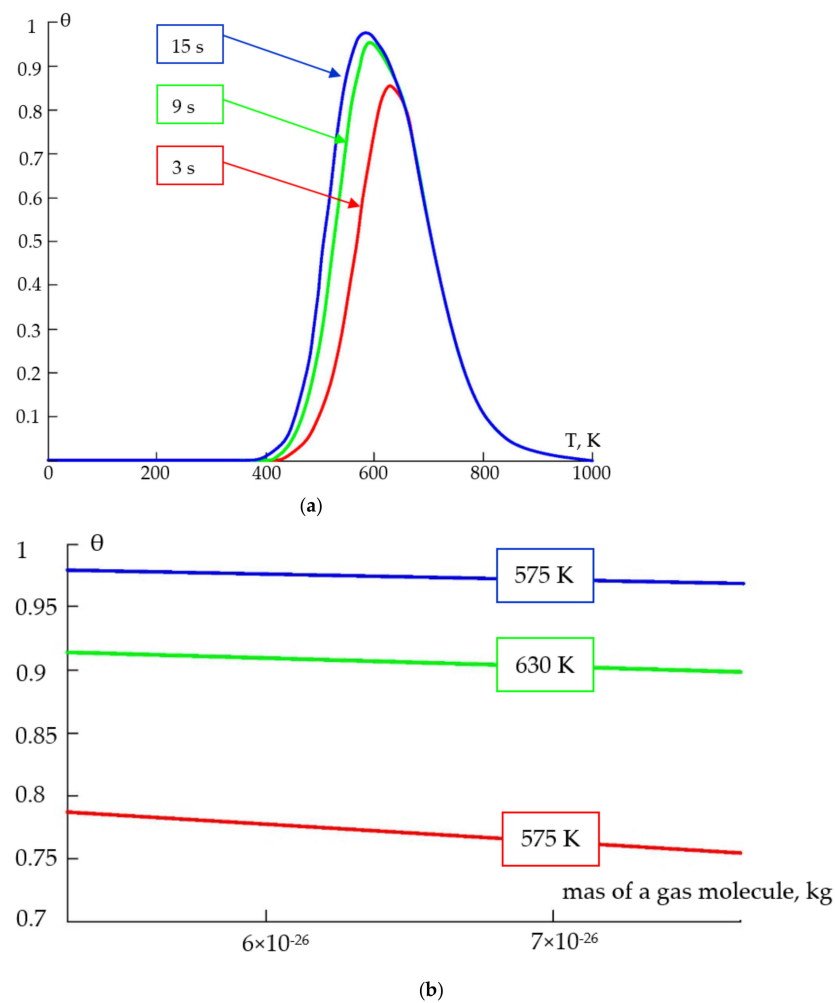


Figure 19. The dependence of degree of filling on temperature at different filling times (a); mass of a gas molecule at different temperatures (b).

To increase the sensitivity $S = (R_{\text{AIR}} - R_{\text{GAS}})/R_{\text{GAS}}$ of the adsorption semiconductor sensory layers, it was considered possible to create a relatively high resistance in air R_{AIR} and a relatively low resistance of structures in the presence of a reagent gas R_{GAS} . This was achieved through the deliberate introduction of indium oxide into a system based on tin and silica dioxides (the introduction of a nonorganic salt of indium at the stage of the preparation of the polymeric sol–solutions). Measurements of the gas sensitivity of nanocomposites based on tin and silica dioxides and indium oxide were carried out using reductional ethanol and acetone vapours. An analysis of these measurements using PPD, an X-ray phase analysis and TGA data resulted in the establishment of the optimal temperature of nanocomposite annealing (700 °C), below which the sensitivity to reductional gases decreased. It must be noted that if the nanocomposites were annealed at a temperature below the optimal one, an anomalous increase in resistance in the presence of reagent gases was observed, which might be explained by the presence of indium chloride in the nanostructures of the salt, which could have significantly reduced the resistance in the samples. The presence of this phase, especially at high temperatures of gas detection, could have caused an anomalous curve in the gas sensitivity graph.

According to the gas sensitivity measurements, it was established that the deliberate introduction of a semiconductor additive of indium oxide into a two-component system, $\text{SiO}_2\text{--SnO}_2$, increased the sensitivity of the nanostructured layers to reductional reagent gases tenfold ($S = 2\text{--}30$ (for the nanocomposites of a two-component system, $\text{SiO}_2\text{--SnO}_2$)).

to $S = 100\text{--}250$ (for the nanocomposites of a three-component system, $\text{SiO}_2\text{--SnO}_2\text{--In}_2\text{O}_3$), which was caused by a relatively high resistance of the samples in air R_{AIR} .

3. Conclusions

The analysis of gas sensitivity measurements based on PPD and X-ray phase analysis data allowed us to find the optimal temperature for annealing nanocomposites of a three-component system, $\text{SiO}_2\text{--SnO}_2\text{--In}_2\text{O}_3$ (700 °C). Based on complex studies of AFM, the BET technique and on previous research [47,48], a hierarchical model of the formation of two-component and three-component porous nanocomposites was proposed, presented in Figures 20 and 21 (in the inset, the semiconductor and dielectric grains of nanocomposites are indicated in pink and blue), accordingly. According to the AFM data, it was found that two-component porous nanocomposites, $\text{SiO}_2\text{--SnO}_2$, were macro-meso-microporous (macropore sizes of 170–180 nm and mesopore sizes of 40–50 nm) and three-component porous nanocomposites, $\text{SiO}_2\text{--SnO}_2\text{--In}_2\text{O}_3$, were meso-microporous (mesopore sizes of 11–15 nm). According to the gas sensitivity measurements, it was established that the deliberate introduction of a semiconductor additive of indium oxide into a two-component system, $\text{SiO}_2\text{--SnO}_2$, increased the sensitivity of the nanostructured layers to reductional reagent gases by tenfold.

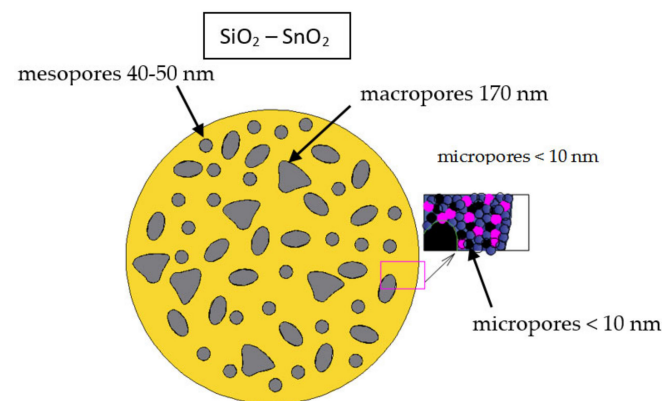


Figure 20. Hierarchical model of the formation of two-component porous nanocomposites.

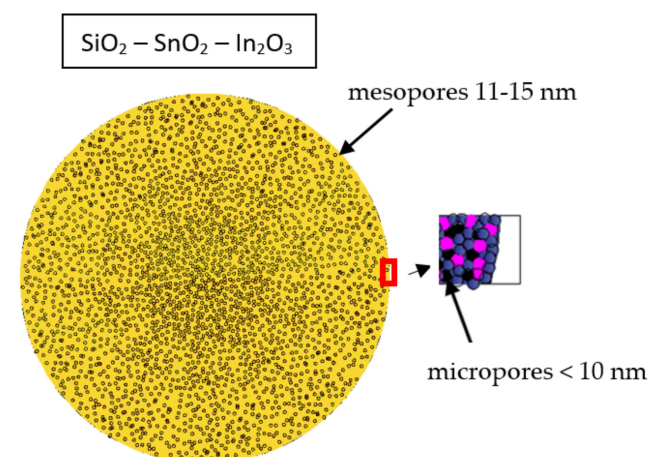


Figure 21. Hierarchical model of the formation of three-component porous nanocomposites.

Based on temperature dependencies (within the temperature range 300–400 °C), the activation energies of sample conductivity were found to be $0.24 \div 0.46$ eV, and the thermal resistance coefficients were found to be $\alpha_R = \frac{1}{R} \frac{\partial R}{\partial T} = -(6 \div 11) \cdot 10^{-3} \text{K}^{-1}$.

A complex analysis of experimental data related to gas sensitivity and the calculation results within the Langmuir and BET models in the integrated LabVIEW system allowed us

to establish the optimal temperature range for the detection process, outside of which the filling degree of the surface for a particular adsorber–adsorbent system decreased, which was shown to be between 300 and 400 °C.

It was shown that for samples characterized by a decrease in sensitivity to reductional gases and in reaction time when the temperature rose within the 250–400 °C range, the ratio of the activation energy for adsorption and desorption was 2.5 to 1, while for porous nanocomposites characterized by the same sensitivity to reductional gases and an insignificant change in reaction time under the same conditions, the ratio was 3.5 to 1.

It was experimentally revealed that the hydrolysis and polycondensation reactions of $\text{Si}(\text{OC}_2\text{H}_5)_4$ in the presence of not one, but two inorganic metal salts ($\text{SnCl}_2 \cdot 2\text{H}_2\text{O}$ and $\text{In}_2(\text{SO}_4)_3$), at the sol preparation stage significantly increased the sensitivity of the porous nanomaterials to reducing gas vapours under the condition of annealing film xerogels at an optimal temperature of 700 °C. Therefore, the addition of indium oxide into a two-component system, $\text{SiO}_2\text{--SnO}_2$, increased the sensitivity of the nanostructured layers to reductional reagent gases at a detection temperature in the range from 300 to 400 °C tenfold ($S = 2\text{--}30$ (for the nanocomposites of a two-component macro–meso–microporous system, $\text{SiO}_2\text{--SnO}_2$) to $S = 100\text{--}250$ (for the nanocomposites of a three-component meso–microporous system, $\text{SiO}_2\text{--SnO}_2\text{--In}_2\text{O}_3$)), which was caused by the samples' relatively high resistance in air R_{AIR} of the latter.

4. Materials and Methods

Tetraethyl orthosilicate $\text{Si}(\text{OC}_2\text{H}_5)_4$, tin (II) chloride and indium (III) sulphate were used as the precursors. The initial components used to create the sols were easily hydrolysed chemicals that, when allowed to interact with water, formed polymolecules or polysolvated groups. Tetraethyl orthosilicate hydrolyse and polycondensation reactions were conducted in the presence of metal oxide sources (inorganic salts, namely, tin (II) chloride and indium (III) sulphate). H_2SO_4 and HCl were added at the stage of dissolving $\text{SnCl}_2 \cdot 2\text{H}_2\text{O}$ and $\text{In}_2(\text{SO}_4)_3$.

Materials based on SiO_2 , SnO_2 and In_2O_3 and produced through sol–gel synthesis were investigated in this study. The source of SiO_2 was $\text{Si}(\text{OC}_2\text{H}_5)_4$ (tetraethoxysilane, TU2637-187-44493179-2014, Moscow, Russia), the source of SnO_2 was $\text{SnCl}_2 \cdot 2\text{H}_2\text{O}$ (GOST 36-78, Saint-Petersburg, Russia) and the source of In_2O_3 was $\text{In}_2(\text{SO}_4)_3$ (TU 6-09-3756-80, Moscow, Russia).

Inorganic salts of tin and indium were dissolved in butyl alcohol until completely dissolved (as a result, transparent solutions were obtained). Then, tetraethyl orthosilicate was added. Two types (xerogel films and xerogel powders) of porous nanocomposites from sols were created.

A water solution of ammonia was used to turn the sols into gels (for creating xerogel powders). The produced wet gel was dried out at a temperature of 100 °C for 50 h and later kept at constant temperatures of 300 °C and 700 °C. To study the xerogel powder samples using X-ray diffraction (XRD, DRON 3.0, Burevestnik, Saint-Petersburg, Russia) and thermal gravimetric analysis (TGA, laboratory installation, St. Petersburg, Russia), the BET (Brunauer–Emmett–Teller) technique was used to determine the surface areas of the xerogel powder samples. The characteristics of the xerogel powders were studied using a gas-adsorbent Sorbi-series analyser (Meta, CJSC, Novosibirsk) by comparing the volumes of the adsorbent gas (nitrogen) adsorbed by the sample, with samples (specific surface area of $106 \text{ m}^2/\text{g}$) provided by Meta, CJSC. As a rule, the plant compatible with the thermodesorption method (TDM) consisted of a gas preparation part (usually tanks filled with N_2 - or Ar-adsorbent gases and He carrier gas), an adsorber, a U-shaped tube, and a gas meter. Adsorbent training happened inside the adsorber, which was placed inside a furnace at a temperature range of 200–350 °C and with He or an Ar/He mixture flowing through. After that, the adsorber was cooled to room temperature with the gas still flowing (at such a temperature, Ar and He normally do not adsorb); then, the adsorber was placed inside a cryogenic storage drawer filled with liquid nitrogen—at this temperature,

Ar was adsorbed, but the carrier gas (He) could practically still not be adsorbed). After equilibrium saturation at a fixed concentration of Ar, the adsorber was heated to room temperature, the Ar adsorbed at 77 K was released and its quantity was measured with a thermal conductivity detector–katharometer.

The xerogel films of the porous nanocomposites of two- and three-component systems (tin dioxide–silica dioxide and tin dioxide–indium oxide–silica dioxide) were formed through the sol–gel method as a result of spinodal decomposition during the application of polymeric sol to the surface of the base and the thermal treatment of structures, during which metal oxides were formed from nonorganic salts, volatile components were actively released (which led to a significant decrease in mass), gels turned into xerogels (thin films) and porous nanomaterials formed under the conditions of spinodal decomposition.

The xerogel films were created from sols. The sols were applied to all substrates using a centrifuge (3000 revolutions per minute) for 3–5 s. The compositions (concentrations) of nanocomposites were chosen as 10SiO₂–90SnO₂, 10SiO₂–85SnO₂–5In₂O₃, 10SiO₂–80SnO₂–10In₂O₃ and 10SiO₂–75SnO₂–15In₂O₃ (mas. %).

Prepared polymer sol solutions were poured onto the surface of substrates pretreated in acetone, isopropyl alcohol and deionized water, and then dispersed using a centrifuge. During centrifugation, a more complete hydrolysis of alkoxides occurred on the substrate surface in a thin sol layer, followed by polycondensation and the formation of spatial structures in the form of gels. Freshly obtained gels are jelly-like products whose inorganic mesh structure retains water, organic solvents and nonreacting substances. During the heat treatment of gels, the following processes occurred: the formation of metal oxides from nonorganic salts; the intensive release of volatile components accompanied by significant weight loss; the compaction of films; improved adhesion of films to the substrate surface; increase in the mechanical and chemical strength of films; the transition of gels into xerogels.

A study of the morphology of film nanostructures synthesized from sols was carried out using semicontact atomic force microscopy (AFM) with the help of the Ntegra Terma nanolaboratory (NT-MDT, Zelenograd, Russia). To test the surface of the produced samples, NSG 01-type probe sensors (resonance frequency of 150 kHz) were used.

The measurement of the gas sensitivity of the film nanocomposite materials produced using the sol–gel method was conducted through measuring the detection temperature and the resistance of sensory nanostructures in an air atmosphere and in the presence of a reagent gas. The two-probe method was used to measure the resistance. The reagent gas concentration was constant. The measurement of the gas sensitivity was performed in stages, first by heating the sensory nanocomposite in a fixed flow of atmospheric air to the required temperature (300–400 °C), measuring the resistance of the active layer at this temperature, and then sending an impulse of the studied material (concentration 1000 ppm) until the resistance of the active layer in the vapours of this material stabilized. The reduction time period was measured from the moment the source of the reagent gas was turned off till the moment when the layer resistance came back to the initial value $\pm 10\%$. The measurement of gas sensitivity was determined using reductional fumes of acetone and ethanol; the sensitivity was measured using the following formula: $S = (R_{AIR} - R_{GAS})/R_{GAS}$, where R_{AIR} is the resistance of the sample in the air and R_{GAS} is its resistance in the presence of a reagent gas.

To understand some of the physical–chemical processes that happen during the adsorption of gas molecules on the surface of the produced nanostructures, two models—the Langmuir model and the Brunauer–Emmett–Teller (BET) theory—were used to carry out calculations in the LabVIEW environment.

We compared the results of a phase analysis of the interaction between components during the formation of nanostructures through the use of X-ray diffraction, the method of partial pressure diagrams in a wide range of temperatures and pressures in a computer mathematics system, Mathcad, and reviewing the results of the measurement of nanocomposite sensitivity.

Author Contributions: I.K., technology, methodology, measurements, writing—review and editing; V.M., development of model concepts, review of publications on the topic of the article; P.K., modeling, creation of software products, model construction, illustrations for the article, editing. All authors have read and agreed to the published version of the manuscript.

Funding: This research received no external funding.

Institutional Review Board Statement: Not applicable.

Informed Consent Statement: Not applicable.

Data Availability Statement: Not applicable.

Conflicts of Interest: The authors declare no conflict of interest.

References

1. Cao, M. Development of Functional Nanomaterials for Applications in Chemical Engineering. *Nanomaterials* **2023**, *13*, 609. [[CrossRef](#)] [[PubMed](#)]
2. Shao, C.; Zhao, H.; Wang, P. Recent development in functional nanomaterials for sustainable and smart agricultural chemical technologies. *Nano Converg.* **2022**, *9*, 11. [[CrossRef](#)] [[PubMed](#)]
3. Wang, Z.; Zhu, L.; Wang, J.; Zhuang, R.; Mu, P.; Wang, J.; Yan, W. Advances in functional guest materials for resistive gas sensors. *RSC Adv.* **2022**, *12*, 24614–24632. [[CrossRef](#)] [[PubMed](#)]
4. Smerdov, R.; Mustafaev, A.; Spivak, Y.; Moshnikov, V. Functionalized Nanostructured Materials for Novel Plasma Energy Systems. In *Topical Issues of Rational Use of Natural Resources 2019*; CRC Press: Boca Raton, FL, USA, 2019; pp. 434–441.
5. Tomaev, V.V.; Stoyanova, T.V. Features of the Growth of Thread-Like $x\text{InSe}(1-x)\text{In}_2\text{O}_3$ Crystals of Two-Layer PbSe and In Films. *Glass Phys. Chem.* **2018**, *44*, 333–338. [[CrossRef](#)]
6. Ghiyasiyan-Arani, M.; Salavati-Niasari, M. Synergic and coupling effect between SnO_2 nanoparticles and hierarchical AlV_3O_9 microspheres toward emerging electrode materials for lithium-ion battery devices. *Inorg. Chem. Front.* **2021**, *8*, 2735–2748. [[CrossRef](#)]
7. Ghiyasiyan-Arani, M.; Salavati-Niasari, M.; Zonouz, A.F. Effect of Operational Synthesis Parameters on the Morphology and the Electrochemical Properties of 3D Hierarchical AlV_3O_9 Architectures for Li-Ion Batteries. *J. Electrochem. Soc.* **2020**, *167*, 2. [[CrossRef](#)]
8. Smerdov, R.; Spivak, Y.; Bizyaev, I.; Somov, P.; Gerasimov, V.; Mustafaev, A.; Moshnikov, V. Advances in Novel Low-Macroscopic Field Emission Electrode Design Based on Fullerene-Doped Porous Silicon. *Electronics* **2020**, *10*, 42. [[CrossRef](#)]
9. Salikhov, K.M.; Stoyanov, N.D.; Stoyanova, T.V. Using Optical Activation to Create Hydrogen and Hydrogen-Containing Gas Sensors. *Key Eng. Mater.* **2020**, *854*, 87–93. [[CrossRef](#)]
10. Tomaev, V.V.; Levine, K.L.; Stoyanova, T.V.; Syrkov, A.G. Synthesis and Study of a Polypyrrole–Aluminum Oxide Nanocomposite Film on an Aluminum Surface. *Glass Phys. Chem.* **2019**, *45*, 291–297. [[CrossRef](#)]
11. Prokopchuk, N.R.; Syrkov, A.G.; Klyuev, A.Y.; Laptik, I.O. Modification of the model compound with nanodiamond particles for precise investment casting of metal articles. *Tsvetnye Met.* **2022**, *6*, 59–63. [[CrossRef](#)]
12. Syrkov, A.G. On the priority of Saint-Petersburg Mining University in the field of nanotechnology science and nanomaterials. *J. Min. Inst.* **2016**, *221*, 730–736. [[CrossRef](#)]
13. Pleskunov, I.V.; Syrkov, A.G. Development of research of low-dimension metal-containing systems from P.P. Weymarn to our days. *J. Min. Inst.* **2018**, *231*, 287–291. [[CrossRef](#)]
14. Budelovskij, D.I.; Yu, P.S.; Lipin, V.A. Peculiarities of Formation and Growth of Nanodispersed Intermetallic Strengthening Inclusions in Rapidly Solidified Alloys of Al-Mg-Zr-X-system. *J. Min. Inst.* **2018**, *230*, 139–145. [[CrossRef](#)]
15. Popova, A.N.; Sukhomlinov, V.S.; Mustafaev, A.S. A new intensity adjustment technique of emission spectral analysis when measured at the upper limit of the dynamic range of charge-coupled devices. *Appl. Sci.* **2022**, *12*, 6575. [[CrossRef](#)]
16. Tomaev, V.V.; Polishchuk, V.A.; Vartanyan, T.A.; Vasil'ev, E.A. Surface Plasmon Resonance in Zinc Nanoparticles. *Glass Phys. Chem.* **2019**, *45*, 238–241. [[CrossRef](#)]
17. Prokopchuk, N.R.; Globa, A.I.; Laptik, I.O.; Syrkov, A.G. The properties of metal coatings enhanced with diamond nanoparticles. *Tsvetnye Met.* **2021**, *6*, 50–54. [[CrossRef](#)]
18. Huang, A.; He, Y.; Zhou, Y.; Zhou, Y.; Yang, Y.; Zhang, J.; Luo, L.; Mao, Q.; Hou, D.; Yang, J. A review of recent applications of porous metals and metal oxide in energy storage, sensing and catalysis. *J. Mater. Sci.* **2019**, *54*, 949–973. [[CrossRef](#)]
19. Brinker, C.J. Hydrolysis and condensation of silicates: Effects on structure. *J. Non-Cryst. Solids* **1988**, *100*, 31–50. [[CrossRef](#)]
20. Brinker, C.J.; Scherer, G.W. Sol-Gel Science. In *The Physics and Chemistry of Sol-Gel Processing*; Academic Press: San Diego, CA, USA, 1990.
21. Varshney, B.; Siddiqui, M.J.; Anwer, A.H.; Khan, M.Z.; Ahmed, F.; Aljaafari, A.; Hammud, H.H.; Azam, A. Scientific Reports. Synthesis of mesoporous SnO_2/NiO nanocomposite using modified sol-gel method and its electrochemical performance as electrode material for supercapacitors. *Sci. Rep.* **2020**, *10*, 11032. [[CrossRef](#)]

22. Patel, M.; Mishra, S.; Verma, R.; Shikha, D. Synthesis of ZnO and CuO nanoparticles via Sol gel method and its characterization by using various technique. *Discov. Mater.* **2022**, *2*, 1. [[CrossRef](#)]
23. Mansour, N.B.; Khouqeer, G.; All, N.A.; Ghoul, J.E. Synthesis of hybrid nanocomposites by sol-gel method and their characterizations. *J. Ovonic Res.* **2022**, *18*, 57–65. [[CrossRef](#)]
24. Lu, X.; Hasegawa, G.; Kanamori, K.; Nakanishi, K. Hierarchically porous monoliths prepared via sol–gel process accompanied by spinodal decomposition. *J. Sol-Gel Sci. Technol.* **2020**, *95*, 530–550. [[CrossRef](#)]
25. Lu, X.; Kanamori, K.; Nakanishi, K. Synthesis of hierarchically porous MgO monoliths with continuous structure via sol–gel process accompanied by phase separation. *J. Sol-Gel Sci. Technol.* **2019**, *89*, 29–36. [[CrossRef](#)]
26. Gheonea, R.; Crasmareanu, E.C.; Plesu, N.; Sauca, S.; Simulescu, V.; Ilia, G. New Hybrid Materials Synthesized with Different Dyes by Sol-Gel Method. *Adv. Mater. Sci. Eng.* **2017**, *2017*, 4537039. [[CrossRef](#)]
27. Bokov, D.; Jalil, A.T.; Chupradit, S.; Suksatan, W.; Ansari, M.J.; Shewael, I.H.; Valiev, G.H.; Kianfar, E. Nanomaterial by Sol-Gel Method: Synthesis and Application. *Adv. Mater. Sci. Eng.* **2021**, *2021*, 5102014. [[CrossRef](#)]
28. Ryu, H.-W.; Park, B.-S.; Akbar, S.A.; Lee, W.-S.; Hong, K.-J.; Seo, Y.-J.; Shin, D.-C.; Park, J.-S.; Choi, G.-P. ZnO sol–gel derived porous film for CO gas sensing. *Sens. Actuators B Chem.* **2003**, *96*, 717–722. [[CrossRef](#)]
29. Inaba, M.; Kono, M.; Oda, T.; Phansiri, N.; Nakano, M.; Suehiro, J. Response properties of nitrogen dioxide gas sensors with tin oxide decorated carbon nanotube channel fabricated by two-step dielectrophoretic assembly. *AIP Adv.* **2020**, *10*, 055223. [[CrossRef](#)]
30. Chai, H.; Zheng, Z.; Liu, K.; Xu, J.; Wu, K.; Luo, Y.; Liao, H.; Debliquy, M.; Zhang, C. Stability of Metal Oxide Semiconductor Gas Sensors: A Review. *IEEE Sens. J.* **2022**, *22*, 5470. [[CrossRef](#)]
31. Mirzaei, A.; Ansari, H.R.; Shahbaz, M.; Kim, J.-Y.; Kim, H.W.; Kim, S.S. Metal Oxide Semiconductor Nanostructure Gas Sensors with Different Morphologies. *Chemosensors* **2022**, *10*, 289. [[CrossRef](#)]
32. Rzaiz, J.M.; Nawaf, S.O.; Ibrahim, A.K. A review on tin dioxide gas sensor: The role of the metal oxide doping, nanoparticles, and operating temperatures. *World J. Adv. Res. Rev.* **2022**, *14*, 51–62. [[CrossRef](#)]
33. Masuda, Y. Recent advances in SnO₂ nanostructure based gas sensors. *Sens. Actuators B Chem.* **2022**, *364*, 131876. [[CrossRef](#)]
34. Acharyya, S.; Nag, S.; Guha, P.K. Ultra-selective tin oxide-based chemiresistive gas sensor employing signal transform and machine learning techniques. *Anal. Chim. Acta.* **2022**, *1217*, 339996. [[CrossRef](#)]
35. Ou, L.-X.; Liu, M.-Y.; Zhu, L.-Y.; Zhang, D.W.; Lu, H.-L. Recent Progress on Flexible Room-Temperature Gas Sensors Based on Metal Oxide Semiconductor. *Nano-Micro Letters.* **2022**, *14*, 206. [[CrossRef](#)]
36. Kong, Y.; Li, Y.; Cui, X.; Su, L.; Ma, D.; Lai, T.; Yao, L.; Xiao, X.; Wang, Y. SnO₂ nanostructured materials used as gas sensors for the detection of hazardous and flammable gases: A review. *Nano Mater. Sci.* **2022**, *4*, 339–350. [[CrossRef](#)]
37. Sharma, A.; Ahmed, A.; Singh, A.; Oruganti, S.K.; Khosla, A.; Arya, S. Review—Recent Advances in Tin Oxide Nanomaterials as Electrochemical/Chemiresistive Sensors. *J. Electrochem. Soc.* **2021**, *168*, 027505. [[CrossRef](#)]
38. Hasan, B.A. SnO₂ doped In₂O₃ thin films as reducing gas sensors. *IOP Conf. Ser.: Mater. Sci. Eng.* **2020**, *928*, 072011. [[CrossRef](#)]
39. Shen, H.; Lib, L.; Xu, D. Preparation of one-dimensional SnO₂–In₂O₃ nanoheterostructures and their gas-sensing property. *RSC Adv.* **2017**, *7*, 33098. [[CrossRef](#)]
40. Pandit, N.A.; Ahmad, T. Tin Oxide Based Hybrid Nanostructures for Efficient Gas Sensing. *Molecules* **2022**, *27*, 7038. [[CrossRef](#)]
41. Tyagi, S.; Chaudhary, M.; Ambedkar, A.K.; Sharma, K.; Gautam, Y.K.; Singh, B.P. Metal oxide nanomaterial-based sensors for monitoring environmental NO₂ and its impact on the plant ecosystem: A review. *Sens. Diagn.* **2022**, *1*, 106–129. [[CrossRef](#)]
42. Isaac, N.A.; Pikaar, I.; Biskos, G. Metal oxide semiconducting nanomaterials for air quality gas sensors: Operating principles, performance, and synthesis techniques. *Mikrochim. Acta.* **2022**, *189*, 196. [[CrossRef](#)]
43. Saruhan, B.; Fomekong, R.L.; Nahirniak, S. Review: Influences of Semiconductor Metal Oxide Properties on Gas Sensing Characteristics. *Front. Sens.* **2021**, *2*, 657931. [[CrossRef](#)]
44. Lun, D.; Xu, K. Recent Progress in Gas Sensor Based on Nanomaterials. *Micromachines* **2022**, *13*, 919. [[CrossRef](#)] [[PubMed](#)]
45. Yang, Y.; Maeng, B.; Jung, D.; Lee, J.; Kim, Y.; Kwon, J.; An, H.K.; Jung, D. Annealing Effects on SnO₂ Thin Film for H₂ Gas Sensing. *Nanomaterials* **2022**, *12*, 3227. [[CrossRef](#)] [[PubMed](#)]
46. Krishna, K.G.; Parne, S.; Pothukanuri, N.; Kathirvelu, V.; Gandi, S.; Joshi, D. Nanostructured metal oxide semiconductor-based gas sensors: A comprehensive review. *Sens. Actuators A Phys.* **2022**, *341*, 113578. [[CrossRef](#)]
47. Kononova, I.; Moshnikov, V.; Kononov, P.; Ignat’ev, S. Fractal-percolation structure architectonics in sol-gel synthesis. *Int. J. Mol. Sci.* **2021**, *22*, 10521. [[CrossRef](#)]
48. Kononova, I.; Kononov, P.; Moshnikov, V. Step-by-Step Modeling and Experimental Study on the Sol–Gel Porous Structure of Percolation Nanoclusters. *Coatings* **2023**, *13*, 449. [[CrossRef](#)]
49. Kulikov, I.S. Thermodynamics of oxides. *Mosc. Metall.* **1986**, 344.

Disclaimer/Publisher’s Note: The statements, opinions and data contained in all publications are solely those of the individual author(s) and contributor(s) and not of MDPI and/or the editor(s). MDPI and/or the editor(s) disclaim responsibility for any injury to people or property resulting from any ideas, methods, instructions or products referred to in the content.